

See discussions, stats, and author profiles for this publication at: <https://www.researchgate.net/publication/232729141>

# Comparison between Dealloyed PtCo<sub>3</sub> and PtCu<sub>3</sub> Cathode Catalysts for Proton Exchange Membrane Fuel Cells

ARTICLE in THE JOURNAL OF PHYSICAL CHEMISTRY C · AUGUST 2012

Impact Factor: 4.77 · DOI: 10.1021/jp306107t

CITATIONS

26

READS

115

8 AUTHORS, INCLUDING:



Zhang Junliang

Universal Technology Corporation

44 PUBLICATIONS 1,825 CITATIONS

SEE PROFILE



Joseph M. Ziegelbauer

General Motors Company

28 PUBLICATIONS 411 CITATIONS

SEE PROFILE



Huolin L Xin

Brookhaven National Laboratory

95 PUBLICATIONS 1,953 CITATIONS

SEE PROFILE



Indrajit Dutta

Corning Incorporated

20 PUBLICATIONS 185 CITATIONS

SEE PROFILE

# Comparison between Dealloyed $\text{PtCo}_3$ and $\text{PtCu}_3$ Cathode Catalysts for Proton Exchange Membrane Fuel Cells

Zhiqiang Yu,<sup>\*,†,‡</sup> Junliang Zhang,<sup>\*,†,○</sup> Zhongyi Liu,<sup>§</sup> Joseph M. Ziegelbauer,<sup>§</sup> Huolin Xin,<sup>||,◆</sup> Indrajit Dutta,<sup>#,||</sup> David A. Muller,<sup>⊥,▽</sup> and Frederick T. Wagner<sup>†</sup>

<sup>†</sup>Electrochemical Energy Research Laboratory, General Motors, Honeoye Falls, New York 14472, United States

<sup>‡</sup>China Science Lab, General Motors, 56 Jinwan Road, Pudong, Shanghai, 201206, PR China

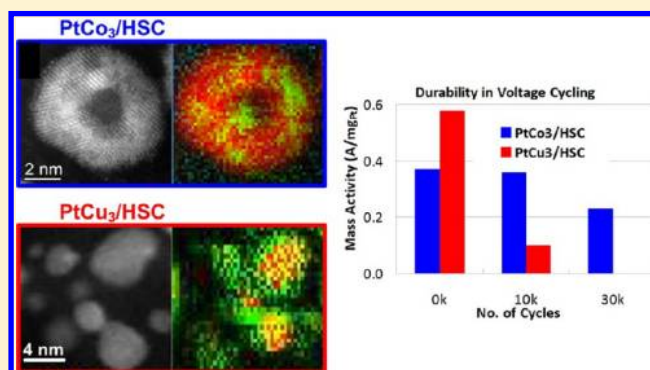
<sup>§</sup>Electrochemical Energy Research Laboratory, General Motors, Warren, Michigan 48090, United States

<sup>||</sup>Department of Physics and <sup>⊥</sup>School of Applied and Engineering Physics, Cornell University, Ithaca, New York 14853, United States

<sup>#</sup>Trison Business Solutions, Inc., Leroy, New York 14482, United States

<sup>▽</sup>Kavli Institute at Cornell for Nanoscale Science, Ithaca, New York 14853, United States

**ABSTRACT:** Dealloyed  $\text{PtCo}_3$  and  $\text{PtCu}_3$  catalysts supported on high surface area carbon (HSC), which were synthesized under different conditions, were tested as cathode electrodes in proton exchange membrane fuel cells. The dealloyed  $\text{PtCu}_3/\text{HSC}$  gave higher initial oxygen reduction reaction (ORR) kinetic activity but much worse durability in a voltage cycling test. Detailed characterization was undertaken to develop insights toward the development of catalysts with both high activity and good durability. In situ X-ray absorption spectroscopy (XAS) analysis showed that dealloyed  $\text{PtCu}_3/\text{HSC}$  exhibited stronger bulk Pt–Pt compressive strains and higher bulk d-band vacancies (attributed in part to a greater ligand effect induced by Pt–Cu bonding) than dealloyed  $\text{PtCo}_3/\text{HSC}$ , factors which can be expected to correlate with the higher initial activity of dealloyed  $\text{PtCu}_3/\text{HSC}$ . Annular dark field (ADF) imaging and electron energy loss spectroscopy (EELS) mapping demonstrated that a strong majority of metal nanoparticles in both dealloyed  $\text{PtCu}_3/\text{HSC}$  and  $\text{PtCo}_3/\text{HSC}$  have variants of core–shell structures. However, the most prevalent structure in the dealloyed  $\text{PtCo}_3/\text{HSC}$  gave multiple dark spots in ADF images, approximately half of which were due to Co-rich alloy cores and half of which arose from voids or surface divots. In contrast, the ADF and EELS data for dealloyed  $\text{PtCu}_3/\text{HSC}$  suggested the predominance of Pt shells surrounding single Cu-rich cores. Further work is needed to determine whether the contrast in durability between these catalysts arises from this observed structural difference, from the differences between the corrosion chemistry of Cu and Co, or from other factors not addressed in this initial comparison between two specific catalysts.



## INTRODUCTION

Proton exchange membrane fuel cells (PEMFCs) have been studied extensively for years for automotive applications due to their high energy efficiency and zero emissions. Nowadays, the large-scale automotive applications of PEMFCs are constrained to a great extent by the large Pt usage as electrocatalysts, particularly in the cathode. Since the hydrogen oxidation reaction (HOR) on the anode is facile, the Pt loading in the anode can be as low as  $0.025 \text{ mg}_{\text{Pt}} \cdot \text{cm}^{-2}$  without contributing measurable kinetic losses.<sup>1</sup> In contrast, the oxygen reduction reaction (ORR) on the cathode is so sluggish that the efforts of generations have been aimed at understanding the ORR mechanism and developing more active ORR catalysts.<sup>2,3</sup> It has been commonly accepted that a target of a 4-fold improvement in ORR activity versus a state-of-the-art Pt/C catalyst having a benchmark ORR activity of  $0.1 \text{ A} \cdot \text{mg}_{\text{Pt}}^{-1}$  has to be met for the

realization of mass-produced automotive applications of PEMFCs.<sup>2</sup>

One approach to the development of more active catalysts has been the use of carbon-supported Pt–M alloy catalysts, where M is a non-noble metal such as Fe, Co, Ni, Cu, or Cr.<sup>4–10</sup> These have typically had the stoichiometry  $\text{Pt}_3\text{M}$  and have historically given ORR activities, per unit Pt mass, 2–3 times higher than the state-of-the-art pure Pt/C catalysts. Strasser and co-workers have shown that making Pt–Cu alloy catalysts with an excess of Cu (typically Cu to Pt atomic ratio at 3) and then removing ~90% of Cu via electrochemical voltage cycling can yield 4–6-fold activity enhancements over the benchmark Pt/C catalyst.<sup>8,9,11–13</sup> They ascribed the increased

Received: June 21, 2012

Revised: July 25, 2012

Published: August 22, 2012

activity to the compression of the Pt lattice in Pt-rich outer shells of the partially dealloyed Pt–Cu nanoparticles.<sup>14</sup> To determine whether the promise of higher activities offered by dealloyed catalysts can be brought to practical fruition in PEMFCs, it is necessary (1) to develop more practical means of removing the excess alloying atoms prior to fabrication of fuel cell electrodes and (2) to evaluate the durability of such catalysts under accelerated stress tests.

The electrochemical dealloying methods employed by Strasser's group, applied to complete electrodes,<sup>8,9</sup> are awkward to implement during the scale-up of catalyst preparation. One must remove at least most of the excess alloying element before making membrane electrode assemblies due to two factors: (1) excess M ions in the membrane interfere with fuel cell operation<sup>15</sup> and (2) postfabrication aqueous processing of complete membrane electrode assemblies (MEAs) leads to MEA wrinkling, which compromises the assembly of leak-free fuel cell stacks. In this work, therefore, dealloying was accomplished by simple chemical leaching of the catalyst powders in aqueous nitric acid prior to MEA fabrication. Nitric acid was chosen because of the greater solubility of copper in oxidizing, as opposed to nonoxidizing, acids.

PEMFCs, particularly during automotive operations, are subjected to load cycles during which Pt-based catalysts become covered with surface oxides [at idle or low power (high potential)], and these oxides are then reduced [at high power (low potential)]. During this voltage cycling a small amount of Pt can dissolve and either redeposit onto larger particles in the cathode catalyst layer or migrate into the membrane and deposit as metallic Pt.<sup>16</sup> Both of these processes lead to a loss of active metal surface, as measured by hydrogen electrosorption. The voltage cycling can also accentuate the removal of non-noble alloying element atoms, M, from the near surface region of alloy or partially dealloyed particles.<sup>5</sup> In this work, we compare the voltage-cycling durability of two catalysts, one prepared from a PtCu<sub>3</sub>/C precursor powder and one prepared from a PtCo<sub>3</sub>/C precursor, as a first step in evaluating the factors that control the durability of Pt–M alloy systems after partial dealloying. Cu and Co have quite disparate standard reduction potentials [0.35 V vs normal hydrogen electrode (NHE) for Cu<sup>2+</sup> and –0.23 V for Co<sup>2+</sup>], and they may have different dissolution rates in both dealloying and voltage cycling. The objective of this work was to compare these two catalysts and try to correlate their activities, durabilities, and detailed nanostructures. This comparison can further assist us in better understanding the origin of the high ORR activity and in designing dealloyed Pt–M catalysts with superior activity and durability.

## ■ EXPERIMENTAL SECTION

The dealloyed PtCo<sub>3</sub>/HSC catalyst was prepared by an impregnation method, followed by high-temperature annealing and then acid leaching. First, a commercial Pt/high-surface carbon (HSC) powder [Tanaka Kikinzoku Kogyo (TKK), 28.1 wt % Pt] was impregnated with an aqueous solution of cobalt chloride (0.4 M) with the atomic ratio Co:Pt of 3 and was dried at 80 °C for 24 h. Second, the dried catalyst powder was annealed at 900 °C in 10 vol % H<sub>2</sub>/N<sub>2</sub> for 5 h to form Pt–Co alloy nanoparticles. Finally, the annealed catalyst powder was leached in 1 M nitric acid at 80 °C for 24 h to remove the excess Co, washed with copious deionized water (18.2 MΩ), dried at 80 °C for 24 h, and then ground manually in a mortar, forming the final dealloyed PtCo<sub>3</sub>/HSC. The dealloyed PtCu<sub>3</sub>/

HSC catalyst precursor was prepared by Strasser's group at the University of Houston using a previously described freeze-drying method and was annealed at 800 °C at the University of Houston.<sup>8,9,17</sup> This catalyst precursor was then chemically dealloyed at GM using 1 M nitric acid at 25 °C for 48 h at room temperature to remove the excess Cu. It then went through the same washing, drying, and grinding procedures as mentioned above to form the final dealloyed PtCu<sub>3</sub>/HSC catalyst.

The metal loadings of the two dealloyed catalysts were measured by an inductively coupled plasma optical emission spectrometer (Varian 725-ES, ICP-OES). The morphologies of Pt–Co and Pt–Cu nanoparticles at the atomic scale were probed using a high-angle annular dark field scanning transmission electron microscope (ADF-STEM, FEI TECNAI F-20). Intensities in ADF images are proportional both to thickness and to the square of the atomic number Z. The latter effect allows one to distinguish between Pt-rich (high Z) and Co- or Cu-rich regions of a particle and also serves to increase the contrast between the metal particles and the carbon support. Electron energy loss spectroscopy (EELS) mapping in a scanning transmission electron microscope (STEM) was performed on the dealloyed PtCo<sub>3</sub>/HSC using an aberration-corrected Nion UltraSTEM microscope at Cornell University to further visualize the nanostructure of Pt–Co nanoparticles at atomic resolution,<sup>18</sup> while EELS mapping of dealloyed PtCu<sub>3</sub>/HSC was conducted on a corrected JEOL 2100 F STEM in the GM research lab in Warren, MI.

In situ X-ray absorption spectroscopy (XAS) measurements were conducted using a spectroelectrochemical cell of a previously described design to probe the structure and Pt d-band vacancies of the catalysts.<sup>19</sup> The electrodes were painted onto Zoltek carbon cloth from a slurry consisting of the respective catalyst powder, Nafion solution, and a 2-propanol/deionized water mixture (18 MΩ). The final dry catalyst ink was 96:4 catalyst powder:Nafion by mass, and the final geometric Pt loadings were 1.5–2.2 mg<sub>Pt</sub>·cm<sup>–2</sup>. Data collection was performed at beamlines X-23A2 and X-18A at the National Synchrotron Light Source (Brookhaven National Laboratory, Upton, NY). The energies of the incident X-ray radiation were set to the Pt L<sub>2</sub> and L<sub>3</sub> edges (13 723 and 11 564 eV, respectively) via monochromators constructed from single crystals of Si(311) and Si(111). Because the data were collected in transmission mode, two to three electrode layers were required to give adequate Pt L<sub>3</sub> and L<sub>2</sub> edge heights. Experimental data were also collected for a Pt reference foil (7 μm thickness) to aid in energy alignment and derivation of the Pt d-band vacancies. EXAFS data analysis was performed with the IFEFFIT software suite.<sup>20</sup> The data were collected during anodic holds (N<sub>2</sub>-sparged 0.1 M HClO<sub>4</sub>, GFS Chemicals) at 0.54 V vs reference hydrogen electrode (RHE) after several 0.05–1.0 V vs RHE voltage cycles. Potentiostatic control was maintained with an EcoChemie PGSTAT302N potentiostat/galvanostat (Metrohm USA). Extensive details regarding the XAS data collection and analysis are reported elsewhere.<sup>10,21,22</sup>

Dealloyed PtCo<sub>3</sub>/HSC and PtCu<sub>3</sub>/HSC catalysts were tested on rotating disk electrodes (RDEs) in a three-electrode cell at room temperature. An Ag/AgCl/KCl (3 M Cl<sup>–</sup>) leak-free electrode was used as a reference, which was in a separate beaker but connected to the container having working and counter electrodes via an ion bridge. A platinum foil served as the counter electrode, and 0.1 M perchloric acid (HClO<sub>4</sub>) was

used as the electrolyte. The potential of the reference electrode vs RHE was calibrated by (i) first using a Pt disk electrode (6-mm diameter, Pine Instrument) as the working electrode and bubbling  $\text{H}_2$  into the electrolyte and then (ii) scanning the potential (i.e., working vs reference) from  $-100$  to  $-320$  mV at  $5 \text{ mV}\cdot\text{s}^{-1}$ . During this potential scanning, the reaction on the Pt disk electrode switched from  $\text{H}_2$  oxidation to  $\text{H}_2$  evolution reactions. The potential at which zero current was produced gave the absolute value of the reference electrode potential vs RHE, which was  $-270$  mV in this work. The potentials in RDE tests are all reported relative to RHE. A catalyst ink consisting of 15 mg of catalyst powder, 12 mL of  $\text{H}_2\text{O}$ , 3 mL of 2-propanol, and 0.06 mL of 5 wt % ionomer solution (water/*n*-propanol weight ratio at 1:1, Dupont) was obtained after 10 min of sonication. Then, 10  $\mu\text{L}$  of catalyst ink was pipetted onto a flat glassy carbon electrode (5-mm diameter, Pine Instrument) to achieve a Pt loading of  $15 \mu\text{g}_{\text{Pt}}\cdot\text{cm}^{-2}$  and was dried in a slow  $\text{N}_2$  flow for 3 h. The resulting catalyst layer on the glassy carbon electrode was first cleaned by cycling the voltage from 0.05 to 1.2 V at the rate of  $1 \text{ V}\cdot\text{s}^{-1}$  for 200 cycles. Then the ORR activity measurement was carried out using an anodic scan from 0.05 to 1.1 V at the rate of  $5 \text{ mV}\cdot\text{s}^{-1}$  while pure  $\text{O}_2$  was bubbled through the electrolyte. The catalytic activity of catalysts is reported in terms of the Pt mass activity in  $\text{A}\cdot\text{mg}_{\text{Pt}}^{-1}$  or the area-specific activity in  $\mu\text{A}\cdot\text{cm}^{-2}_{\text{Pt}}$  at 0.9 V vs RHE. The reported RDE data of each catalyst were averaged on data from six electrodes, which were made from two separate inks.

Following the RDE tests, both dealloyed  $\text{PtCo}_3/\text{HSC}$  and  $\text{PtCu}_3/\text{HSC}$  catalysts were employed to fabricate cathode electrodes in MEAs for fuel cell performance and durability tests. In this study, MEAs were built with the catalyst coated membrane (CCM) structure using Meyer rod coating and then decal transfer. The cathode catalyst powder and an ionomer solution with a 28.6 wt % solid weight percent and an equivalent weight (EW) of 925 were ball-milled in a mixture of propanol and water (propanol/water weight ratio at 4:1) for 72 h. The weight ratio of ionomer to carbon (I/C ratio) was fixed at 0.95 to ensure good coating quality. The prepared cathode inks were then coated by the Meyer rod coating method on blank ethylenetetrafluoroethylene (ETFE) films to give a Pt loading of  $0.2 \text{ mg}_{\text{Pt}}\cdot\text{cm}^{-2}$  (note that  $\text{cm}^2$  refers to the geometric area of electrodes). The anode electrode with a Pt loading of  $0.05 \text{ mg}_{\text{Pt}}\cdot\text{cm}^{-2}$  and I/C ratio of 0.6 was prepared on an ETFE substrate in a similar procedure. The die-cut cathode- and anode-catalyst-coated decals with an active area of  $50 \text{ cm}^2$  were hot pressed onto a  $25 \mu\text{m}$  Nafion-111 membrane (NRE211, 1100 EW,  $\text{EW} = g_{\text{polymer}}\cdot\text{mol}^{-1}_{\text{H}^+}$ , Dupont) at  $140^\circ\text{C}$ . Carbon paper with a proprietary microporous layer served as gas diffusion media (GDM), and “dog-bone” flow fields emulating flow conditions in full-active-area fuel cell stacks were employed.

The above-prepared  $50 \text{ cm}^2$  MEAs were tested for their cathode ORR kinetic activities using  $\text{H}_2/\text{O}_2$  (anode/cathode), their overall fuel cell performance (i.e., polarization curves) using  $\text{H}_2/\text{air}$ , and their voltage-cycling durabilities at  $80^\circ\text{C}$ . In  $\text{H}_2/\text{O}_2$  tests, the stoichiometries for anode and cathode were 2.0 and 9.5, respectively; the relative humidity was kept at 100%; and the cell total pressure was maintained at  $150 \text{ kPa}_{\text{abs}}$ . The current density was controlled, sequentially, at 0.02, 0.03, 0.05, 0.1, 0.2, and  $0.4 \text{ A}\cdot\text{cm}^{-2}$  for 4–6 min at each point. The stabilized cell voltage was averaged over the last 1 min of this hold. The catalytic activity of the cathode catalysts was

evaluated at a high frequency resistance (HFR)-corrected voltage of 0.9 V vs RHE at  $80^\circ\text{C}$ . In the measurement of  $\text{H}_2/\text{air}$  fuel cell performance, the stoichiometries for anode and cathode were 1.5 and 2.0, respectively; the current density was controlled sequentially at 0.05, 0.2, 0.4, 0.8, 1.0, 1.2, and  $1.5 \text{ A}\cdot\text{cm}^{-2}$  for 4 min stabilization at each point; and data were averaged over the last 1 min. The  $\text{H}_2/\text{air}$  polarization curves with 32% and 100% inlet RH were taken: here they are denoted as fuel cell power module (FCPM) and wet-fuel cell power module (Wet-FCPM), respectively. In voltage cycling tests, 200 sccm  $\text{H}_2$  into anode and 50 sccm  $\text{N}_2$  into cathode were admitted at  $150 \text{ kPa}_{\text{abs}}$ . The cell voltage was swept at  $50 \text{ mV}\cdot\text{s}^{-1}$  between 0.6 and  $1.0 \text{ V}_{(\text{RHE})}$  in a triangle profile for up to 30 000 cycles. The MEAs were subjected to the cathode catalytic activity ( $\text{H}_2/\text{O}_2$ ) and the  $\text{H}_2/\text{air}$  performance tests at 0 cycles [i.e., the beginning of life (BOL)], 10 000 cycles, and 30 000 cycles [i.e., the end of life (EOL)] of voltage cycling. The electrochemical surface areas (ECAs) of the cathode catalysts were obtained from hydrogen-adsorption/desorption (HAD) analysis by integrating hydrogen adsorption area from 0.08 to  $0.4 \text{ V}_{(\text{RHE})}$  in cyclic voltammetry.

## RESULTS AND DISCUSSION

ICP results in Table 1 show that dealloyed  $\text{PtCo}_3/\text{HSC}$  had 24.7 wt % Pt and 2.8 wt % Co, while dealloyed  $\text{PtCu}_3/\text{HSC}$  had

**Table 1. Metal Loadings Measured by ICP**

catalyst	Pt (wt %)	M (wt %)	Pt/M atomic ratio
dealloyed $\text{PtCo}_3/\text{HSC}$	24.7	2.8	2.7
dealloyed $\text{PtCu}_3/\text{HSC}$	28.0	5.6	1.6

$28.0 \text{ wt } \% \text{ Pt}$  and  $5.6 \text{ wt } \% \text{ Cu}$ . The atomic ratios of Pt to base metal in the dealloyed  $\text{PtCo}_3/\text{HSC}$  and  $\text{PtCu}_3/\text{HSC}$  were thus calculated to be 2.7 and 1.6, respectively. Figure 1 displays SEM images of dealloyed  $\text{PtCo}_3/\text{HSC}$  and  $\text{PtCu}_3/\text{HSC}$  catalyst powders. Both catalysts had two distinct types of particles,  $<10 \text{ nm}$  ones and  $>20 \text{ nm}$  ones (as evidenced by the large bright spots in Figures 1a, 1c, and 1d), with the  $<10 \text{ nm}$  particles being in the vast majority. Note a few  $>20 \text{ nm}$  particles are due to the heterogeneous nature of the catalyst preparation method, and the similar large particles are also present in commercial PtCo catalysts (SEM images are not shown). Figure 1 also indicates that the  $<10 \text{ nm}$  particles in dealloyed  $\text{PtCo}_3/\text{HSC}$  seem slightly larger than their counterparts in dealloyed  $\text{PtCu}_3/\text{HSC}$ , which could be due to the higher annealing temperature in dealloyed  $\text{PtCo}_3/\text{HSC}$  relative to that in dealloyed  $\text{PtCu}_3/\text{HSC}$  ( $900$  vs  $800^\circ\text{C}$ ).

Table 2 summarizes ECA, mass activity (MA), and specific activity (SA) of dealloyed  $\text{PtCo}_3/\text{HSC}$  and  $\text{PtCu}_3/\text{HSC}$  catalysts in RDE tests. Dealloyed  $\text{PtCo}_3/\text{HSC}$  exhibited similar HAD area (i.e., ECA) to, but lower MA and SA than, dealloyed  $\text{PtCu}_3/\text{HSC}$ . Following the RDE tests, both catalysts were subjected to MEA tests with voltage cycling from 0.6 to  $1.0 \text{ V}_{(\text{RHE})}$ , and the MAs obtained from the  $\text{H}_2/\text{O}_2$  polarization curves after different stages of voltage cycling are also plotted in Figure 2. At BOL, dealloyed  $\text{PtCu}_3/\text{HSC}$  showed significantly higher MA than dealloyed  $\text{PtCo}_3/\text{HSC}$ , which is consistent with the RDE results. Figure 2 also shows that, during the voltage cycling test, the superior MA of dealloyed  $\text{PtCu}_3/\text{HSC}$  dropped quickly from  $0.58$  to  $0.1 \text{ A}\cdot\text{mg}_{\text{Pt}}^{-1}$  after only 10K cycles. Due to this poor performance, the voltage cycling test for dealloyed  $\text{PtCu}_3/\text{HSC}$  was stopped after 10K cycles. In



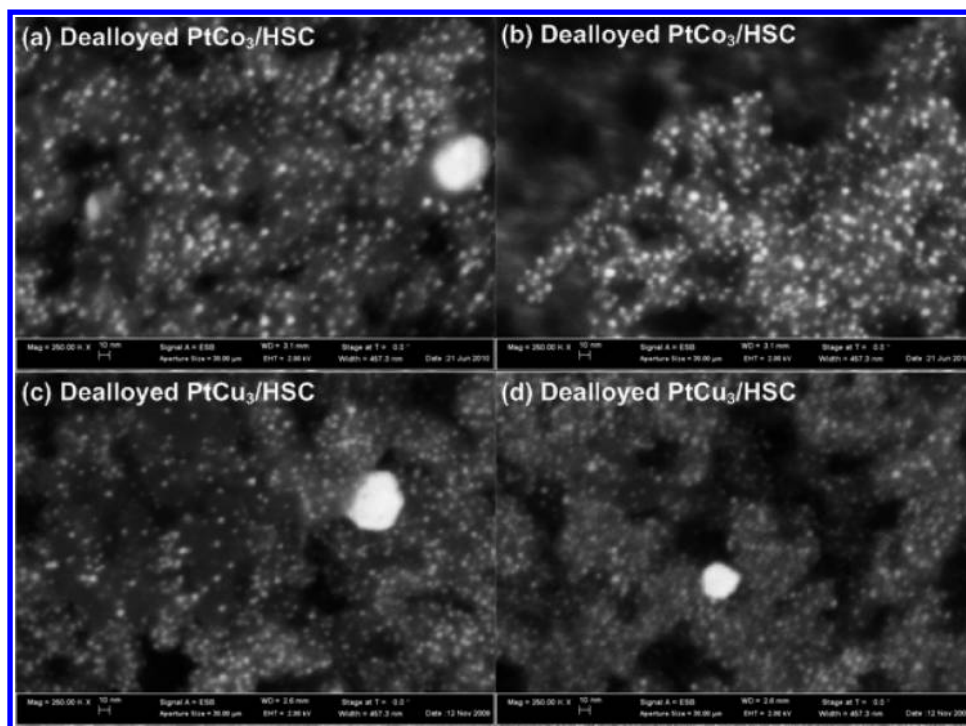


**Figure 1.** SEM images of (a, b) dealloyed PtCo<sub>3</sub>/HSC and (c, d) dealloyed PtCu<sub>3</sub>/HSC catalyst powders. The scale bars are 10 nm. Three large spots (in a, c, and d) represent three large Pt particles, respectively.

**Table 2.** RDE Results

catalyst	ECA (m <sup>2</sup> ·g <sup>-1</sup> <sub>Pt</sub> )	MA (A·mg <sup>-1</sup> <sub>Pt</sub> )	SA (μA·cm <sup>-2</sup> <sub>Pt</sub> )
dealloyed PtCo <sub>3</sub> /HSC	62	0.396	635
dealloyed PtCu <sub>3</sub> /HSC	68	0.558	824

contrast, dealloyed PtCo<sub>3</sub>/HSC exhibited almost no degradation in MA as voltage cycling reached 10K cycles, and its MA remained well above 0.2 A·mg<sup>-1</sup><sub>Pt</sub> after 30K cycles, which was still approximate 2 times the benchmark Pt/C catalyst of about 0.1 A·mg<sup>-1</sup><sub>Pt</sub>.<sup>2</sup>

The development of ORR catalysts with superior Pt mass activities requires striking a balance between two competing influences: (i) the sufficient O<sub>2</sub> adsorption and the O–O bond breaking, and (ii) the facile removal of adsorbed oxygen species (such as O<sub>ad</sub> and OH<sub>ad</sub>).<sup>4,23</sup> It has been proposed that dealloyed Pt–M catalysts take on a Pt<sub>shell</sub>/PtM<sub>core</sub> structure, in which the mismatch between the lattice constants in Pt shell and Pt–M core induces compressive strains in the Pt shell.<sup>14</sup> The alloying base metal (M) beneath the Pt shell can also impose ligand effects onto the Pt shell, which shifts the Pt d-band center lower relative to the Fermi level and increases the d-band vacancy of Pt atoms in the Pt shell.<sup>14</sup> But the ligand effects are reported to become negligible as the thickness of the Pt shell increases beyond four Pt monolayers, equivalent to about 1 nm.<sup>7</sup> Both compressive strains and ligand effects can cause a decrease in the Pt–O bond strength, thereby resulting in higher turnover frequency of ORR.<sup>4,6,7,24</sup> However, determination of the relative importance of compressive strains and ligand effects in conferring the better ORR activity remains elusive. In this study, in situ XAS was used to determine the bulk d-band vacancies of the Pt atoms at 0.54 V vs RHE and the average Pt–Pt interatomic distances in the catalysts. Detailed descriptions of the methodologies to obtain these two values

are reported in ref 10. Table 3 lists the bulk average Pt–Pt interatomic distance ( $R_{\text{Pt-Pt}}$ ) and the bulk d-band vacancies of Pt atoms in the dealloyed PtCo<sub>3</sub>/HSC and PtCu<sub>3</sub>/HSC catalysts and, for comparison, in a bulk Pt foil. It shows that both dealloyed catalysts exhibited lower  $R_{\text{Pt-Pt}}$  and higher d-band vacancies than the bulk Pt foil, manifesting the alloying effects as expected. Compared with dealloyed PtCo<sub>3</sub>/HSC, dealloyed PtCu<sub>3</sub>/HSC showed lower  $R_{\text{Pt-Pt}}$  and higher d-band vacancies. Mukerjee et al. reported that the enhanced Pt activities for Pt–M alloy catalysts had been correlated to the increased Pt d-band vacancies deduced from the in situ XAS analysis.<sup>22</sup> Thus, from the results in Table 3 one would expect the dealloyed PtCu<sub>3</sub>/HSC to be more active than the dealloyed PtCo<sub>3</sub>/HSC, as observed. However, Strasser et al. contended that a strained pure Pt shell should have a lower d-band vacancy and have ascribed the increased Pt activities to the Pt lattice compression of the Pt shell of the dealloyed particles.<sup>14</sup> Note that in situ XAS is a bulk-averaging technique and thereby generates the bulk d-band vacancies of Pt atoms in the whole dealloyed particles, whereas the d-band vacancy that Strasser et al. reported was more toward the Pt shell in the dealloyed particles. The electron microscopy results that followed showed that dealloyed PtCo<sub>3</sub>/HSC and PtCu<sub>3</sub>/HSC catalysts differ in structural details in ways that can affect the relationships between the average  $R_{\text{Pt-Pt}}$  and average d-band vacancies discussed here and the surface and near-surface properties that more directly impact catalytic behavior. More detailed analyses of the X-ray absorption data for dealloyed PtCu<sub>3</sub>/HSC and PtCo<sub>3</sub>/HSC catalysts will be reported elsewhere.<sup>25,26</sup>

To further investigate the origin of the activity and durability differences between these catalysts, nanostructures of dealloyed PtCo<sub>3</sub>/HSC and PtCu<sub>3</sub>/HSC were examined by ADF-STEM and EELS mapping. As mentioned above, dealloyed Pt–M catalysts take on a basically similar Pt<sub>shell</sub>/PtM<sub>core</sub> structure. However, their nanostructures can vary in the overall catalyst

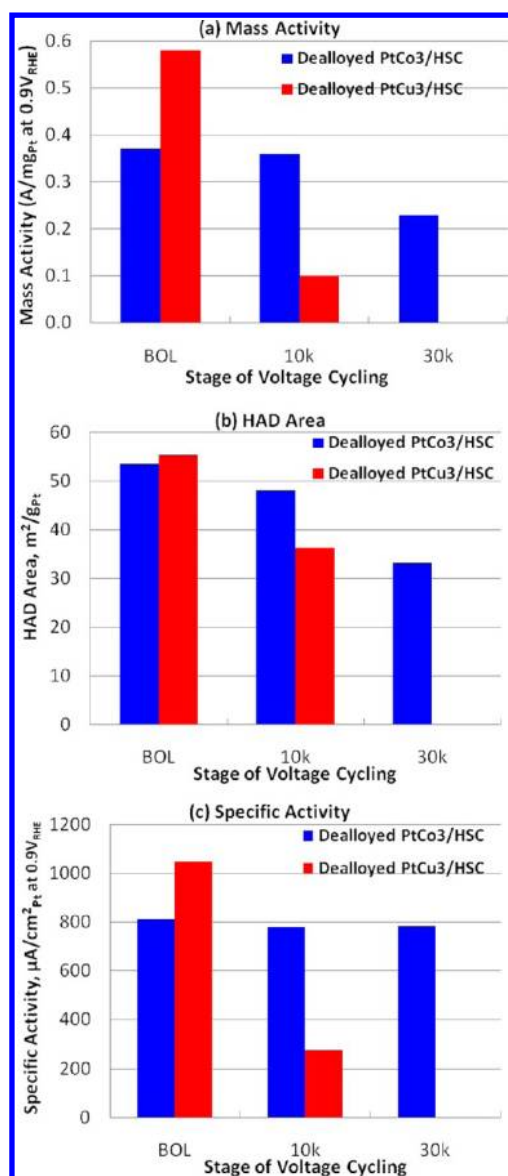


**Figure 2.** (a) Mass activities, (b) HAD areas, and (c) specific activities of dealloyed PtCo<sub>3</sub>/HSC (in blue) and PtCu<sub>3</sub>/HSC (in red) catalysts during the voltage cycling tests of MEAs. Conditions: 80 °C, 100% RH, 50 sccm H<sub>2</sub> in anode, 200 sccm N<sub>2</sub> in cathode, voltage range of 0.6–1.0 V (vs RHE), and scan rate at 50 mV·s<sup>−1</sup>.

**Table 3.**  $R_{\text{Pt-Pt}}$  (interatomic distance in bulk) and Bulk d-Band Vacancy at 0.54 V<sub>(RHE)</sub> from XAS

catalyst	$R_{\text{Pt-Pt}}$ (Å)	d-band vacancy <sup>a</sup>
bulk Pt foil	2.776	0.300
dealloyed PtCo <sub>3</sub> /HSC	2.733	0.329
dealloyed PtCu <sub>3</sub> /HSC	2.700	0.363

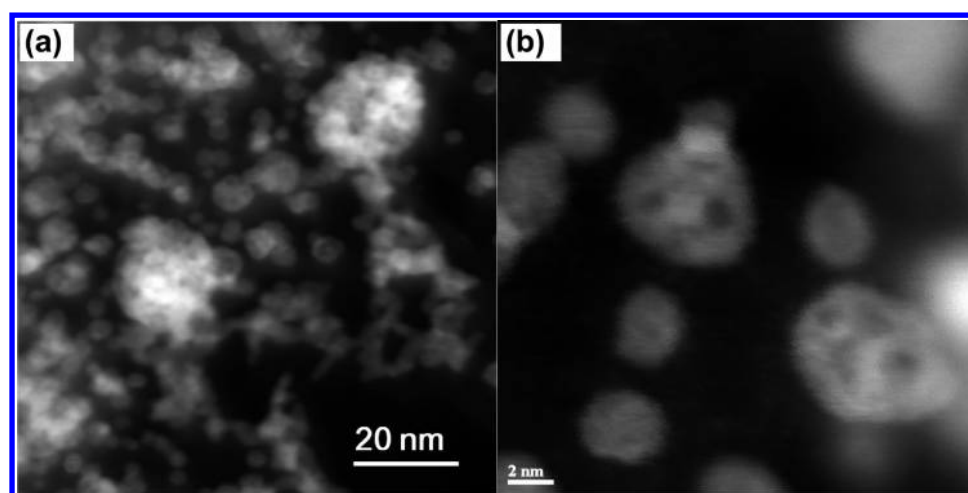
<sup>a</sup>: The calculations for the d-band vacancy of bulk Pt are from refs 31, 32.

particle size, the Pt<sub>shell</sub> thickness, as well as the morphology and composition of the inner PtM<sub>core</sub> (such as homogeneous vs heterogeneous). Figure 3a,b shows ADF images of dealloyed PtCo<sub>3</sub>/HSC. The images suggest that the majority of particles (including both <10 and >20 nm particles) in dealloyed PtCo<sub>3</sub>/HSC have significant intensity variations (dark spots), with several dark spots within each of the vast majority of the

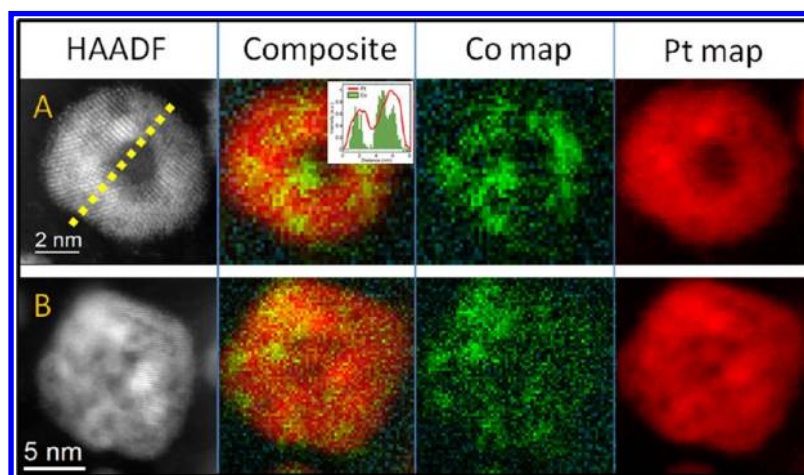
particles. Figure 4 shows EELS mappings of particles with multiple dark spots in dealloyed PtCo<sub>3</sub>/HSC. Similar-appearing images with multiple dark spots varying in size from the angstrom level to ~2 nm had been reported for large particles of a commercial Pt<sub>3</sub>Co catalyst by the Shao-Horn group.<sup>5</sup> They reported that the multiple dark ADF spots in that commercial catalyst corresponded to empty spaces or voids within the particle, and they hypothesized that this structure arose from the presence of excess Co in the larger precursor particles of the catalyst precursor, leading to a porous “percolated” structure after acid leaching. However, a detailed analysis of ADF and EELS-mapping images of the dealloyed PtCo<sub>3</sub>/HSC under discussion in this work suggests that the “dark spots” can be either Co-rich regions (due to the lower atomic number of Co vs Pt) or real voids. The average probability for a “dark spot” to be a real void rather than a Co-rich core was 42% ± 15% (95% confidence level) in this catalyst.<sup>27</sup> The Co maps in Figure 4 further indicate that the Co distribution is not homogeneous throughout the entire structure, even excluding the voids. Rather, several different areas of local concentration of Co are often seen within a particle. These particles are therefore best described as Pt<sub>shell</sub>/multi-PtCo<sub>core</sub> particles containing some voids. The EELS line scan inserted in Figure 4 clearly shows a Pt<sub>shell</sub>/multi-PtCo<sub>core</sub> structure. From Figure 4, it appears that the thickness of Pt outside of the individual Pt–Co cores is variable and in some places may be less than 1 nm.

Figure 5a,b shows the ADF images of dealloyed PtCu<sub>3</sub>/HSC. Compared to those in dealloyed PtCo<sub>3</sub>/HSC, the majority of particles <10 nm in dealloyed PtCu<sub>3</sub>/HSC did not evidence multiple “dark spots” within single particles. Figure 6 displays another ADF image of dealloyed PtCu<sub>3</sub>/HSC and the EELS mappings of particles in the red frame. The composite elemental mapping clearly indicates that the core is Pt–Cu alloy and the shell is pure Pt. Although the resolution of the EELS mapping used for dealloyed PtCu<sub>3</sub>/HSC in Figure 6 was worse than that for dealloyed PtCo<sub>3</sub>/HSC in Figure 4 due to use of a different microscope, results in Figures 5 and 6 demonstrate that the particles (particular those <10 nm) in dealloyed PtCu<sub>3</sub>/HSC predominantly have relatively homogeneous core composition and thus are considered to have a Pt<sub>shell</sub>/single-PtCu<sub>core</sub> structure.

Both the dealloyed PtCo<sub>3</sub>/HSC and the dealloyed PtCu<sub>3</sub>/HSC catalysts discussed here were prepared via synthesis routes involving addition of aqueous solutions of the alloying element to a commercial Pt/C catalyst, annealing the alloying-element precursor in H<sub>2</sub> to mix and alloy the metals, and then dealloying via acid leaching, though there were significant differences in preparative detail. One might expect some level of heterogeneity in the particles generated by these processes, as evidenced by the presence of many small particles and a few large particles in each catalyst. In addition, a minority of small particles in each catalyst showed the structure predominant in the other catalyst. For instance, while dealloyed PtCo<sub>3</sub>/HSC is best described as having Pt<sub>shell</sub>/multi-PtCo<sub>core</sub> nanostructures, it can be discerned in Figure 3b that a few particles (typically <5 nm and constituting a small fraction of the total observed particles) in dealloyed PtCo<sub>3</sub>/HSC catalyst present no obvious “dark spots” inside. Detailed EELS mappings (not shown here) have indicated that these minority particles have a single-core–shell structure with a uniform Pt–Co core and two to three monolayers of Pt as a shell.<sup>27</sup> Similarly, although the majority of small particles in dealloyed PtCu<sub>3</sub>/HSC appeared to have the Pt<sub>shell</sub>/single-PtCu<sub>core</sub> structure, two medium-sized particles



**Figure 3.** ADF images of dealloyed  $\text{PtCo}_3/\text{HSC}$  catalyst powder. Fields of vision were chosen to include some large particles  $>20$  nm, which were not common in this catalyst.



**Figure 4.** EELS maps of two typical dealloyed  $\text{PtCo}_3/\text{HSC}$  catalyst nanoparticles (A and B) showing the multiple Pt–Co cores. The gray images are the HAADF images recorded with the same probe settings but higher pixel density than the EELS maps. An example of EELS line scan (corresponding to the dashed yellow line in the HAADF image of particle A) is also included as an inset in the composite image of particle A. The EELS line scan clearly shows a  $\text{Pt}_{\text{shell}}/\text{multi-PtCo}_{\text{core}}$  structure. Recorded on 100 keV Nion UltraSTEM.

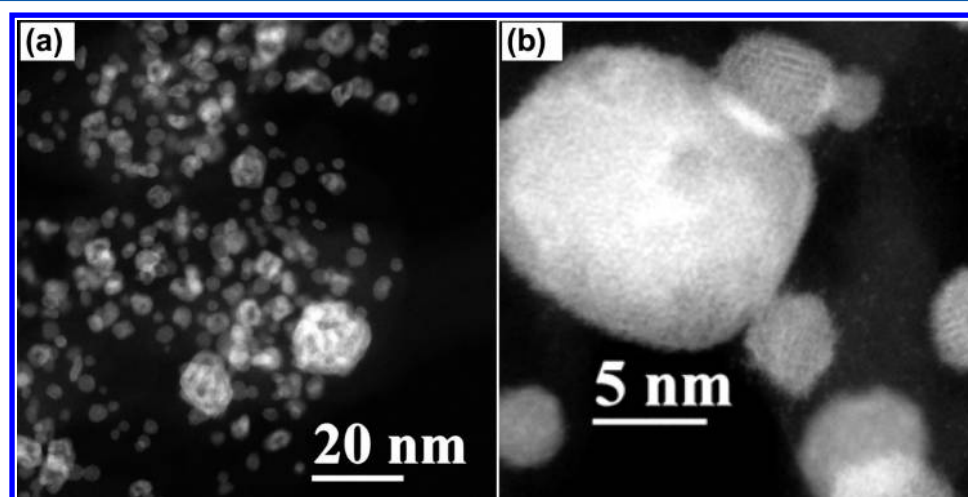


**Figure 5.** ADF images of dealloyed  $\text{PtCu}_3/\text{HSC}$  catalyst powder. Fields of vision were chosen to include some large particles  $>15$ – $20$  nm, which were not common in this catalyst.

( $>10$  nm) in Figure 5a are observed to have multiple dark spots, suggesting  $\text{Pt}_{\text{shell}}/\text{multi-PtCu}_{\text{core}}$  nanostructures. Oezaslan

et al.<sup>28</sup> have reported that, in  $\text{PtCu}_3/\text{HSC}$  and  $\text{PtCo}_3/\text{HSC}$  catalysts dealloyed by an electrochemical process (rather than



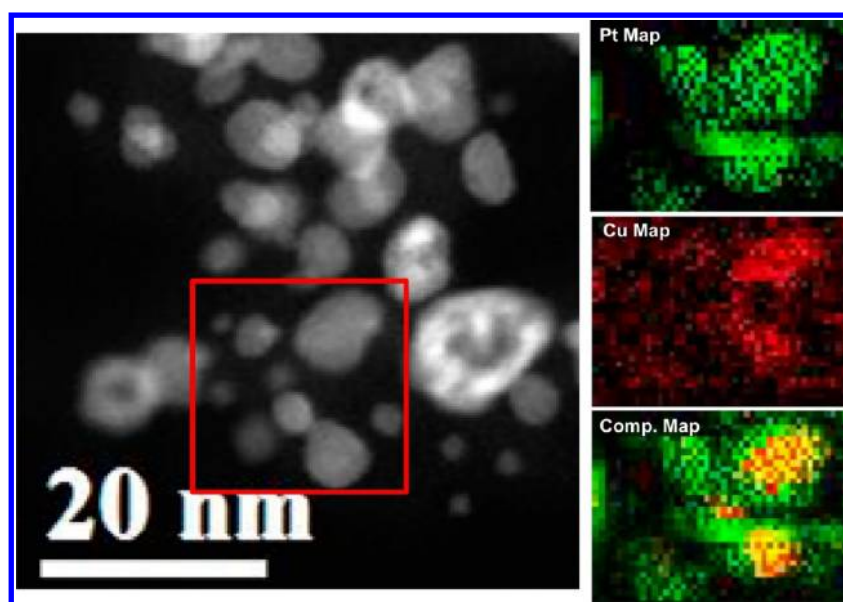


**Figure 6.** ADF image and EELS mappings of dealloyed  $\text{PtCu}_3/\text{HSC}$  catalyst powder showing the  $\text{Pt}_{\text{shell}}/\text{single-PtCu}_{\text{core}}$  structure. Gray image is the ADF image for the particle under the mapping analysis. Green indicates the Pt mapping, red indicates the Cu mapping, and yellow indicates Pt–Cu mixtures.

the chemical processes used here), the particle morphology correlates simply with particle size. They reported single-core/shell structures for particles <10–15 nm, multiple-core/shell structures for particles between 15 and 30 nm, and porous multiple-core/shell structures for particles >30 nm. While our microscopic effort did not specifically look to test for a size/structure correlation, our images seem to suggest a somewhat more complex situation for our chemically dealloyed catalysts.

It is tempting to think that the greater prevalence of multicore particles in the dealloyed  $\text{PtCo}_3/\text{HSC}$  than in the dealloyed  $\text{PtCu}_3/\text{HSC}$  of this work might lead to the observed greater durability of the ORR kinetic activity of the dealloyed  $\text{PtCo}_3/\text{HSC}$ . Both Co and Cu are soluble in acidic electrolytes over the potential ranges experienced in operating fuel cells. One would expect that durability is conferred by the corrosion resistance of the Pt shell surrounding the alloying-element-rich (M-rich) cores. Any single break in the Pt shell around a single core could allow leaching of M from the core and loss of specific activity. In a multiple-core particle, one would require multiple breaks in the Pt shell to allow total removal of M from the particle. Comparisons between additional pairs of single- and multiple-core particles are needed to test this hypothesis.

A possible alternate explanation for the observed greater kinetic stability of dealloyed  $\text{PtCo}_3/\text{HSC}$  vs dealloyed  $\text{PtCu}_3/\text{HSC}$  lies in the possibility of partial passivation of Co in acid media. Copper is more noble than Co (sharing a much broader domain of thermodynamic immunity to reaction with water) and is more resistant to corrosion than Co in nonoxidizing acids, at least when coupled to a metal with a low hydrogen evolution overpotential such as Pt. However, Co and Ni have very similar Pourbaix diagrams and therefore can be expected to have very similar corrosion behavior.<sup>29</sup> Pourbaix notes that Ni shows a broader domain of passivation by oxides than would be expected from the thermodynamics of the bulk metal, oxide, and solution phases. Experimentally, Ni gives passive corrosion currents of several to several tens of  $\mu\text{A}\cdot\text{cm}^{-2}$  in dilute nonoxidizing acids over much of the fuel cell potential range, though it reverts to active dissolution near the hydrogen

evolution potential.<sup>30</sup> This passivation likely arises from the greater thermodynamic stability of the surface oxide than of bulk NiO or  $\text{Ni}(\text{OH})_2$ . A similar partial passivation of Co may limit the progressive removal of Co from the dealloyed  $\text{PtCo}_3/\text{HSC}$  catalyst during voltage cycling. Further analysis is required to determine the extent to which surface Co oxides may contribute to the comparative better stability of dealloyed  $\text{PtCo}_3/\text{HSC}$ .

With the assumption of continuous Co dissolution during voltage cycling, one would reasonably expect that the specific activity of dealloyed  $\text{PtCo}_3/\text{HSC}$  should gradually decrease in a manner similar to its mass activity. However, Figure 2c shows that the specific activity of dealloyed  $\text{PtCo}_3/\text{HSC}$  remained nearly constant as the voltage cycling progressed. Since the specific activity is defined as the current at HFR-corrected voltage of 0.9  $V_{\text{(RHE)}}$  normalized to ECA, the unchanged specific activity during voltage cycling is likely due to a near-perfect compensation of activity decrease with cobalt loss with a specific activity increase accompanying the observed increase in particle size (i.e., decrease in ECA as shown in Figure 2b). Similar observations have also been reported for other cycled Pt–M alloy catalysts.<sup>5,8</sup> In Figure 2c, the specific activity of dealloyed  $\text{PtCo}_3/\text{HSC}$  was nearly constant at about  $800 \mu\text{A}\cdot\text{cm}^{-2}_{\text{Pt}}$ , equivalent to an approximately 4-fold enhancement over the benchmark Pt/C catalyst with a specific activity of  $210 \mu\text{A}\cdot\text{cm}^{-2}_{\text{Pt}}$ . This result indicates that enough Co must be still present inside the Pt–Co nanoparticles of dealloyed  $\text{PtCo}_3/\text{HSC}$  at EOL to support the high specific activity. Therefore, more detailed compositional and structural analyses of the cycled Pt–Co nanoparticles and of other aged dealloyed catalysts are needed to elucidate the origin of the high specific activity remaining at EOL. This analysis should in turn assist us in better understanding the evolution of Pt–Co nanoparticles during voltage cycling and determine where alloying Co should reside with respect to the Pt–Co nanoparticles for superior voltage cycling durability.

During operation of a fuel cell some non-noble-element atoms dissolve out of Pt-alloy catalysts and pass as mobile ions



into the membrane. The reduction potential of  $\text{Cu}^{2+}$  (but not of  $\text{Co}^{2+}$ ) is higher than the reversible hydrogen potential of the fuel cell anode. There is thus the possibility of  $\text{Cu}^{2+}$  migrating through the membrane and getting plated as Cu metal onto the anode. To test this possibility, the anode of a MEA made with dealloyed  $\text{PtCu}_3/\text{HSC}$  as the cathode catalyst was subjected to cyclic voltammetry (CV) following the voltage cycling test. The anode CVs in Figure 7 clearly show the presence of a bulk Cu

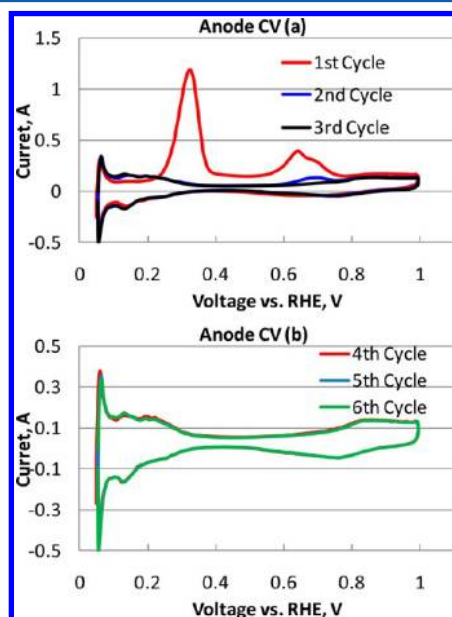


**Figure 7.** Cyclic voltammetry of the anode of the MEA made with dealloyed  $\text{PtCu}_3/\text{HSC}$  as the cathode catalyst following the voltage cycling test. Six consecutive CVs are shown here.

stripping peak centered on 0.35 V and an underpotential deposition (UPD) Cu peak centered on 0.6–0.7 V in the first positive-going sweep (first cycle in Figure 7a). Both of these peaks disappeared completely after the third anodic sweep. Integration of the charge associated with the UPD-Cu peak, assuming one Cu atom per surface Pt atom,  $2 e^-$  per Cu atom, and  $210 \mu\text{C}\cdot\text{cm}^{-2}_{\text{Pt}}$  shows that the anode Pt catalyst is almost fully covered by plated UPD-Cu. If the plated bulk Cu is also included in the calculation, the total Cu stripping charge is 5 times the amount needed to cover the anode Pt catalyst completely. Since the Cu covering on the anode catalyst was so significant, calculation on HOR kinetics was conducted and showed that an assumed 98% Cu coverage on the anode catalyst would lead to 10 mV HOR overpotential at the current of  $0.1 \text{ A}\cdot\text{cm}^{-2}$  (in the proximity of which current, ORR activities were measured), which would then diminish the ORR activity measurements in MEAs by about 40%. Despite the negative effect of Cu deposition on the  $\text{PtCu}_3/\text{HSC}$  ORR measurements, the conclusion drawn from Figure 2 that dealloyed  $\text{PtCu}_3/\text{HSC}$  showed worse durability toward voltage cycling compared with dealloyed  $\text{PtCo}_3/\text{HSC}$  remains valid. The nearly full covering of the anode catalyst by plated Cu would further inhibit HOR and increase the anode potential when the fuel cell is operated at high current density. This poisoning of the anode, coupled with the poor durability of the ORR kinetics of dealloyed  $\text{PtCu}_3/\text{HSC}$ , is driving the development of dealloyed catalysts using nonprecious metals other than Cu.

## SUMMARY

Dealloyed  $\text{PtCo}_3/\text{HSC}$  and  $\text{PtCu}_3/\text{HSC}$  catalysts were synthesized, characterized, and tested as the cathode electrode in PEMFCs. For the majority of particles, which have sizes  $<10$  nm, dealloyed  $\text{PtCu}_3/\text{HSC}$  showed a  $\text{Pt}_{\text{shell}}/\text{single-PtCu}_{\text{core}}$  structure, whereas dealloyed  $\text{PtCo}_3/\text{HSC}$  dominantly showed a  $\text{Pt}_{\text{shell}}/\text{multi-PtCo}_{\text{core}}$  structure (with a small fraction of the  $\text{Pt}_{\text{shell}}/\text{single-PtCo}_{\text{core}}$  structure). For the much-less-numerous particles  $>20$  nm, both of these two catalysts gave particles showing multiple dark spots by ADF microscopy. In situ XAS analysis showed that dealloyed  $\text{PtCu}_3/\text{HSC}$  exhibited higher bulk Pt–Pt compressive strain in addition to higher bulk Pt d-band vacancies than dealloyed  $\text{PtCo}_3/\text{HSC}$ , correlating with its higher initial ORR activity over that of dealloyed  $\text{PtCo}_3/\text{HSC}$ . MEA tests showed that this dealloyed  $\text{PtCu}_3/\text{HSC}$  catalyst had much worse durability toward voltage cycling compared with this dealloyed  $\text{PtCo}_3/\text{HSC}$  catalyst. The relatively high voltage cycling durability of dealloyed  $\text{PtCo}_3/\text{HSC}$  may be due to the formation of Co oxide-like species on the catalyst surface, thereby suppressing the Co dissolution and maintaining the alloying effect. The observed Cu plating on the anode, coupled with the poor durability of dealloyed  $\text{PtCu}_3/\text{HSC}$ , is driving the development of dealloyed catalysts using nonprecious metals other than Cu. More analysis of the cycled dealloyed  $\text{PtCo}_3/\text{HSC}$  is needed to elucidate the origin of the relatively high ORR activity at EOL and thus help design dealloyed catalysts with superior durability.

## AUTHOR INFORMATION

### Corresponding Author

\*E-mail: zhiqiang.yu@gm.com; junliang.zhang@sjtu.edu.cn.

### Present Addresses

<sup>○</sup>Energy Research Institute, School of Mechanical Engineering, Shanghai Jiao Tong University, Shanghai 200240, PR China.

<sup>◆</sup>Lawrence Berkeley National Lab, Berkeley, CA 94720, United States.

<sup>‡</sup>Corning Inc., Corning, New York, United States.

### Notes

The authors declare no competing financial interest.

## ACKNOWLEDGMENTS

We thank Michael Flanagan, Stacy Downs, Travis Downs, Ted Gacek, and Mohammed Atwan for technical support. We also thank Prof. Peter Strasser for providing the dealloyed  $\text{PtCu}_3/\text{HSC}$  catalyst precursor and Prof. Jonah Erlebacher for helpful discussions. This work was partially funded by the Energy Efficiency and Renewable Energy Office of the U.S. Department of Energy (DOE) under contract DE-EE0000458. Use of the National Synchrotron Light Source, Brookhaven National Laboratory, was supported by the DOE, Office of Science, Office of Basic Energy Sciences (BES), under Contract No. DE-AC02-98CH10886. We would also like to acknowledge the support of the Industrial Research Program of the Photon Sciences Directorate of Brookhaven National Laboratory. Use of the Advanced Photon Source, an Office of Science User Facility operated for the DOE Office of Science by Argonne National Laboratory, was supported by the U.S. DOE under Contract No. DE-AC02-06CH11357. Work at Cornell and HLX was supported by the Energy Materials Center at Cornell, a DOE Energy Frontier Research Center (BES contract No. DE-SC0001086). Electron microscopy facilities at the Cornell Center for Materials Research (CCMR) are supported by the

National Science Foundation Materials Research Science and Engineering Centers (MRSEC) program (DMR 1120296).

## ■ REFERENCES

- (1) Wagner, F. T.; Lakshmanan, B.; Mathias, M. F. *J. Phys. Chem. Lett.* **2010**, *1*, 2204.
- (2) Gasteiger, H. A.; Kocha, S. S.; Sompalli, B.; Wagner, F. T. *Appl. Catal., B* **2005**, *56*, 9.
- (3) Zhang, J.; Sasaki, K.; Sutter, E.; Adzic, R. R. *Science* **2007**, *12*, 220.
- (4) Stamenkovic, V. R.; Mun, B. S.; Arenz, M.; Mayrhofer, K. J. J.; Lucas, C. A.; Wang, G.; Ross, P. N.; Markovic, N. M. *Nat. Mater.* **2007**, *6*, 241.
- (5) Chen, S.; Gasteiger, H. A.; Hayakawa, K.; Tada, T.; Shao-Horn, Y. *J. Electrochem. Soc.* **2010**, *157*, A82.
- (6) Gasteiger, H. A.; Markovic, N. M. *Science* **2009**, *324*, 48.
- (7) Chen, S.; Sheng, W.; Yabuuchi, N.; Ferreira, P. J.; Allard, L. F.; Shao-Horn, Y. *J. Phys. Chem. C* **2009**, *113*, 1109.
- (8) Neyerlin, K. C.; Srivastava, R.; Yu, C.; Strasser, P. *J. Power Sources* **2009**, *186*, 261.
- (9) Mani, P.; Srivastava, R.; Strasser, P. *J. Phys. Chem. C* **2008**, *112*, 2770.
- (10) Dutta, I.; Carpenter, M. K.; Balogh, M. P.; Ziegelbauer, J. M.; Moylan, T. E.; Atwan, M. H.; Irish, N. P. *J. Phys. Chem. C* **2010**, *114*, 16309.
- (11) Hasché, F.; Oezaslan, M.; Strasser, P. *ChemCatChem* **2011**, *3*, 1805.
- (12) Mani, P.; Srivastava, R.; Strasser, P. *J. Power Sources* **2011**, *196*, 666.
- (13) Oezaslan, M.; Strasser, P. *J. Power Sources* **2011**, *196*, 5240.
- (14) Strasser, P.; Koh, S.; Anniyev, T.; Greeley, J.; More, K.; Yu, C.; Liu, Z.; Kaya, S.; Nordlund, D.; Ogasawara, H.; Toney, M. F.; Nilsson, A. *Nat. Chem.* **2010**, *2*, 454.
- (15) Greszler, T. A.; Moylan, T. E.; Gasteiger, H. A. *Modeling the Impact of Cation Contamination in a Polymer Electrolyte Membrane Fuel Cell. Handbook of Fuel Cells*; Wiley: New York, 2010.
- (16) Ferreira, P. J.; la O, G. J.; Shao-Horn, Y.; Morgan, D.; Makharia, R.; Kocha, S.; Gasteiger, H. A. *J. Electrochem. Soc.* **2005**, *152*, A2256.
- (17) Srivastava, R.; Mani, P.; Strasser, P. *J. Power Sources* **2009**, *190*, 40.
- (18) Xin, H. L.; Mundy, J. A.; Liu, Z.; Cabezas, R.; Hovden, R.; Kourkoutis, L. F.; Zhang, J.; Subramanian, N. P.; Makharia, R.; Wagner, F. T.; Muller, D. A. *Nano Lett.* **2012**, *12*, 490.
- (19) Arruda, T. M.; Shyam, B.; Ziegelbauer, J. M.; Mukerjee, S.; Ramaker, D. E. *J. Phys. Chem. C* **2008**, *112*, 18087.
- (20) Newville, M. *J. Synchrotron Radiat.* **2001**, *8*, 322.
- (21) Mukerjee, S.; Srinivasan, S.; Soriaga, M. P.; McBreen, J. *J. Phys. Chem.* **1995**, *99*, 4577.
- (22) Mukerjee, S.; Srinivasan, S.; Soriaga, M. P.; McBreen, J. *J. Electrochem. Soc.* **1995**, *142*, 1409.
- (23) Wang, J. X.; Uribe, F. A.; Springer, T. E.; Zhang, J.; Adzic, R. R. *Faraday Discuss.* **2008**, *140*, 1.
- (24) Ziegelbauer, J. M.; Zhang, J.; Dutta, I. *GM Internal Report EER 10-28*; GM: Warren, MI, 2010.
- (25) Jia, Q.; Trahan, M.; Caldwell, K.; Ziegelbauer, J. M.; Ramaker, D. E.; Mukerjee, S. Manuscript in preparation, 2012.
- (26) Ziegelbauer, J. M.; Zhang, J.; Dutta, I. Submitted, 2012.
- (27) Liu, Z.; Xin, H.; Yu, Z.; Zhu, Y.; Zhang, J.; Mundy, J. A.; Muller, D.; Wagner, F. T. *J. Electrochem. Soc.* **2012**, *159*, F554.
- (28) Oezaslan, M.; Heggen, M.; Strasser, P. *J. Am. Chem. Soc.* **2011**, *134*, 514.
- (29) M. Pourbaix *Atlas of Electrochemical Equilibria in Aqueous Solutions*, 2nd ed.; Natl Assn of Corrosion: Houston, TX, 1974.
- (30) Wagner, F. T.; Moylan, T. E. *J. Electrochem. Soc.* **1989**, *136*, 2498.
- (31) Brown, M.; Peierls, R. E.; Stern, E. A. *Phys. Rev. B* **1977**, *15*, 738.
- (32) Mattheiss, L. F.; Dietz, R. E. *Phys. Rev. B* **1980**, *22*, 1663.